






Galilean invariant dynamics in an emergent spin-orbit coupled Zeeman lattice

M. K. H. Ome ¹, Huaxin He², A. Mukhopadhyay ¹, E. Crowell¹, S. Mossman ¹, T. Bersano¹, Yongping Zhang ²✉ & P. Engels ¹✉

Periodic band structures are a hallmark phenomenon of condensed matter physics. While often imposed by external potentials, periodicity can also arise through the interplay of couplings that are not necessarily spatially periodic on their own, but this option is generally less explored than the fully-periodic counterpart. Here, we investigate dynamics in a lattice structure that emerges from the simultaneous application of Raman and radio frequency coupling to a dilute-gas Bose-Einstein condensate. We elaborate on the role of Galilean invariance in this system and demonstrate a variety of techniques, including Bloch oscillations and lattice shaking with spin and momentum resolved measurements. This combined coupling scheme allows for tunability and control, enabling future investigations into unconventional band structures such as quasi-flat ground bands and those with semimetal-like band gaps.

¹Department of Physics and Astronomy, Washington State University, Pullman, Washington 99164, USA. ²Department of Physics, Shanghai University, Shanghai 200444, China. ✉email: yongping11@t.shu.edu.cn; engels@wsu.edu

Periodic band structures and spin–orbit coupling play a key role in many modern condensed matter contexts. Implementing these aspects with ultracold quantum gases using optical lattices^{1–4} and Raman dressing⁵ has opened up avenues for research providing deep insights into topics including synthetic gauge fields^{6–9}, optical flux lattices¹⁰, topological state spaces^{11,12}, supersolids^{13–15}, and more^{16–22}.

Supplementing the Raman-dressing-induced spin–orbit coupling with a suitably chosen radio frequency (RF) drive leads to the emergence of an effective lattice structure even though neither the spin–orbit coupling nor the RF alone produces a periodic structure^{23–25}. This synthesized system possesses spin–orbit coupling and a lattice. The lattice is spin-dependent and is called a *Zeeman lattice*. A static version of the spin–orbit coupled Zeeman lattice was first introduced in the pioneering works by²³ and²⁴ for bosonic and fermionic systems, respectively. The dynamical control of a bipartite spin–orbit coupled Zeeman lattice leads to geometrical pumping²⁵. These benchmark investigations witness the powerful amalgamation of the spin–orbit coupling and periodic band structures. Compared to these previous studies, here we extend the treatment of Zeeman lattices to an accelerating case where questions regarding the Galilean invariance of the system become important.

Periodic band structures can be implemented separately for spin–orbit coupled atoms by optical lattices⁷. Such spin–orbit coupled optical lattice systems have been an important platform to predict novel spin states²⁶, engineer energy band geometry²⁷, and explore spin–orbit coupled dynamics such as novel Bloch oscillation²². However, the lack of Galilean invariance in spin–orbit coupled systems^{7,16,28,29} greatly reduces the controllability of optical lattices and strongly limits applications.

In our system, we find that the spin–orbit coupled Zeeman lattice restores Galilean invariance. Accelerating the atoms by an external force can be substituted by appropriate changes of the Raman drive frequency. We exploit this feature to investigate dynamics and demonstrate experimental techniques to manipulate the lattice. We induce Bloch oscillations via an acceleration of the Zeeman lattice, and spectroscopically probe inter-band transitions by shaking the lattice resonantly. With the restoration of Galilean invariance, this work shows that the Zeeman lattice provides a flexible and robust system for manipulating spin–orbit coupled atoms by equivalently tuning the Raman lasers.

Results

Theoretical framework of a Zeeman lattice. A spin–orbit coupled Zeeman lattice is realized via the simultaneous coupling of two hyperfine states ($|\uparrow\rangle$ and $|\downarrow\rangle$) using two separate methods: a pair of Raman lasers and an external RF field. The couplings produced by the Raman lasers and by the RF drive are schematically demonstrated in the bare (uncoupled) basis in Fig. 1a. The Raman beams (marked Ω_R in Fig. 1b) are arranged such that they induce spin–orbit coupling by imparting momentum on the atoms while also flipping the spins in a two-photon transition. The RF coupling flips the spins without changing the momentum state. Then the coupled states, separated in momentum space by the Raman momentum, can interfere, leading to a periodic structure.

This coupling scheme is described by the Hamiltonian²³

$$H_0 = \frac{p_x^2}{2m} + \begin{bmatrix} -\Delta\epsilon/2 & C \\ C^* & \Delta\epsilon/2 \end{bmatrix}, \quad (1)$$

where $C = \frac{\hbar\Omega_R}{2} \exp[i(2k_R x + \varphi(t))] + \frac{\hbar\Omega_{RF}}{2} \exp(i\omega_{RF} t)$. Ω_R is the two-photon Rabi frequency due to the Raman coupling, Ω_{RF} is the RF Rabi frequency, ω_{RF} is the angular frequency of the RF

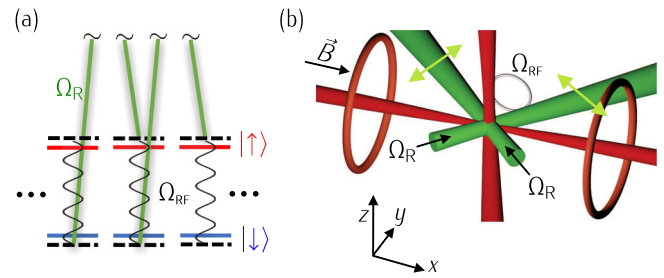


Fig. 1 Zeeman lattice coupling scheme and experimental setup.

a Coupling scheme employed to generate the spin–orbit coupled Zeeman lattice. The horizontal direction indicates momentum, with a spacing of two Raman momenta between adjacent states. Ω_R is the two-photon Rabi frequency due to the Raman coupling (illustrated by the green lines), while Ω_{RF} is the RF Rabi frequency (black wiggly lines). $|\uparrow\rangle$ and $|\downarrow\rangle$ are the hyperfine states (red and blue lines, respectively), with dashed black lines indicating the corresponding detuned states. **b** Schematic of the experimental configuration. Two Raman beams (green beams, marked Ω_R) are incident on the center of a crossed optical dipole trap (red beams) at approximately 45° angles relative to the x -axis. The polarization vectors (colored light green) are perpendicular to the corresponding wave vectors and lie in the xy -plane. The dark brown coils are the bias coils (marked \vec{B}). The gray circle corresponds to the RF antenna (marked Ω_{RF}).

field, and \hbar is the reduced Planck constant. The Raman coupling involves a momentum exchange of $2\hbar k_R$ between the atoms and the Raman beams, where k_R is the effective wave vector of Raman lasers. The energy unit associated with the recoil of the atom due to the absorption of a photon is the recoil energy given by $E_R = \hbar^2 k_R^2 / 2m$. The phase $\varphi(t)$ is connected to the angular frequency difference between the Raman lasers $\Delta\omega_R$, which can readily be tuned in the experiment, $\varphi(t) = \int_0^t d\tau \Delta\omega_R(\tau)$. In the Hamiltonian H_0 , m is the atomic mass and $\Delta\epsilon$ is the energy difference between the two Zeeman states due to the Zeeman shift of an external 10 G bias field (see Experimental setup for details). Without the RF coupling, the spatial dependence in C generates spin–orbit coupling⁵, but effectively there is no lattice structure. Due to the presence of RF coupling, the spatial dependence cannot be gauged out, therefore leaving the signature of the spin–orbit coupled Zeeman lattice.

In order to show the spin–orbit coupled Zeeman lattice explicitly, we apply the unitary transformation $U = \exp[i(2k_R x + \varphi(t))\sigma_z/2]$ ⁵ to the Hamiltonian H_0 in Eq. (1), leading to $H = U^\dagger H_0 U - i\hbar U^\dagger \partial U / \partial t$ with

$$H = \frac{p_x^2}{2m} + \frac{1}{2} \{ \mathbf{B}_{\text{latt}}[x + x_0(t)] + \mathbf{B}_{\text{soc}} \} \cdot \mathbf{S}. \quad (2)$$

Here, $\mathbf{S} = (\sigma_x, \sigma_y, \sigma_z)$ are the Pauli matrices. The Zeeman lattice is spin-dependent and is denoted by $\mathbf{B}_{\text{latt}}[x] = (b_x, b_y, b_z)$ with $b_x = \hbar\Omega_R + \hbar\Omega_{RF} \cos(2k_R x)$, $b_y = \hbar\Omega_{RF} \sin(2k_R x)$, and the detuning $b_z = \hbar d\varphi/dt - \Delta\epsilon = \hbar\Delta\omega_R - \Delta\epsilon$. The time-dependent position offset is $x_0(t) = (\varphi(t) - \omega_{RF} t) / 2k_R$. Therefore, the moving velocity of the Zeeman lattice is

$$v_{\text{lat}} = \frac{dx_0}{dt} = \frac{\Delta\omega_R(t) - \omega_{RF}}{2k_R}. \quad (3)$$

The spin–orbit coupling is represented by $\mathbf{B}_{\text{soc}} = (0, 0, 2\hbar k_R p_x / m)$. The combination of $\mathbf{B}_{\text{latt}}[x]$ and \mathbf{B}_{soc} in the Hamiltonian H represents the spin–orbit coupled Zeeman lattice. If the RF coupling is switched off, then there is no Zeeman lattice. The Zeeman lattice becomes stationary when $\varphi(t) = \int_0^t d\tau \Delta\omega_R(\tau) = \omega_{RF} t$ which implies $b_z = \hbar\omega_{RF} - \Delta\epsilon$. The stationary Zeeman lattice

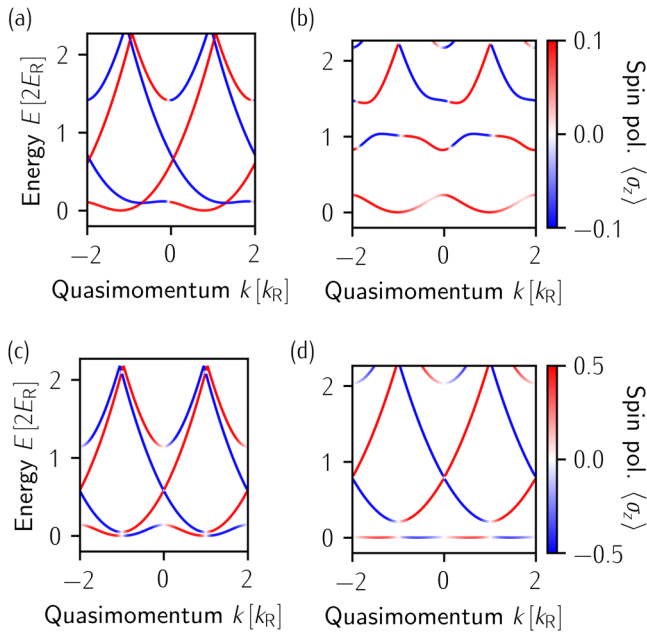


Fig. 2 Band structure over two Brillouin zones where the plot colors indicate the spin polarization $\langle \sigma_z \rangle$. **a** Band structure with spin-orbit coupling in the absence of RF coupling. The parameters are $\hbar\Omega_R = 2.6 E_R$, $\hbar\Omega_{RF} = 0$ and the detuning $b_z = h \times 500$ Hz. **b** Band structure of the stationary Zeeman lattice as described in Eq. (2). The values used in this figure are $\hbar\Omega_R = 2.6 E_R$, $\hbar\Omega_{RF} = 2.3 E_R$ and the detuning $b_z = h \times 500$ Hz. **c** Semimetal-like band structure in the Zeeman lattice. The values used in this figure are $\hbar\Omega_R = 2.0 E_R$, $\hbar\Omega_{RF} = 0.10 E_R$ and the detuning $b_z = 0$ Hz. **d** Flat band in the Zeeman lattice. The values used in this figure are $\hbar\Omega_R = 4.0 E_R$, $\hbar\Omega_{RF} = 0.48 E_R$ and the detuning $b_z = 0$ Hz.

can be realized by tuning the angular frequency difference $\Delta\omega_R$ between the Raman lasers to exactly equal ω_{RF} , which has been explored in^{23,24}.

The lattice structure of the above stationary spin-orbit-RF coupled Hamiltonian [Eq. (2)] can have a meaningful spectrum which has been presented in²⁴. Fig. 2 shows the band structure of the stationary Zeeman lattice in various parameter regimes where the spin polarization $\langle \sigma_z \rangle$ is indicated by the color of the curve and given by $\langle \sigma_z \rangle = (N_\uparrow - N_\downarrow)/N_{\text{tot}}$. Here, N_\uparrow and N_\downarrow are the occupation of the spin up $|\uparrow\rangle$ and spin down $|\downarrow\rangle$ state, respectively, and $N_{\text{tot}} = N_\uparrow + N_\downarrow$. If one applies Bloch's theorem to diagonalize the spin-orbit coupling Hamiltonian (without the RF coupling) assuming an infinite set of plane wave solutions, one finds that bands in different Brillouin zones are not coupled and therefore are trivially inaccessible, shown in Fig. 2a. In other words, this shows that there is no lattice structure in the Raman-induced spin-orbit coupling. The inclusion of the RF coupling then opens up gaps and produces a periodic band structure [cf. Fig. 2b]. The Hamiltonian H given above can be tuned in highly flexible ways. For example, it can result in a semimetal-like band structure [Fig. 2c] or in a nearly flat band as the lowest Bloch band [Fig. 2d] in different parameter regimes.

Galilean symmetry of the Zeeman lattice. It is well-known that spin-orbit coupling breaks Galilean invariance^{7,16,28,30}. Our analysis of the synthesized spin-orbit coupled Zeeman lattice reveals that this lattice restores the Galilean invariance in the following sense: For the Zeeman lattice in Eq. (2), the time-dependence relates to both the Raman lasers and the RF field, i.e., $x_0(t) = (\varphi(t) - \omega_{RF}t)/2k_R$. We can transform into a frame that is

co-moving with the lattice by applying the unitary transformation $G^{31,32}$,

$$G = \exp\left(i\frac{m}{2\hbar} \int_0^t \left(\frac{dx_0(\tau)}{d\tau}\right)^2 d\tau\right) \exp\left(-i\frac{m}{\hbar} \frac{dx_0}{dt} x\right) \exp\left(i\frac{x_0 p_x}{\hbar}\right), \quad (4)$$

which can be considered as a generalized Galilean transformation, since $x_0(t)$ may be time-dependent arbitrarily³³. With $G^\dagger x G = x - x_0$ and $G^\dagger p_x G = p_x - m dx_0/dt$, the resultant Hamiltonian in the co-moving frame is $H_{\text{com}} = G^\dagger H G - i\hbar G^\dagger \partial G/\partial t$ given by

$$H_{\text{com}} = \frac{p_x^2}{2m} + \frac{1}{2} \{ \mathbf{B}'_{\text{latt}}[x] + \mathbf{B}_{\text{soc}} \} \cdot \mathbf{S} + \mathcal{F}x. \quad (5)$$

Here $\mathbf{B}'_{\text{latt}}[x] = (b'_x, b'_y, b'_z)$ with $b'_z = \hbar\omega_{RF} - \Delta\epsilon$, and b'_x and b'_y are as in Eq. (2). Note that $\mathbf{B}'_{\text{latt}}[x]$ is exactly the same as for the stationary Zeeman lattice $[\varphi(t) = \omega_{RF}t]$ in Eq. (2). An arbitrary acceleration of the Zeeman lattice leaves its Hamiltonian invariant up to an additional term which represents the apparent force due to the motion of the noninertial reference frame given by $\mathcal{F} = -m d^2 x_0/dt^2 = -(m/2k_R) d^2 \varphi/dt^2$. Therefore, this analysis reveals that applying an external force to the spin-orbit coupled atoms in a stationary Zeeman lattice is equivalent to accelerating the Zeeman lattice without an external force when viewed from the non-inertial reference frame of the lattice. This equivalence is taken as a signature of the restored Galilean invariance in the system, even though it is in the presence of the spin-orbit coupling.

From an experimental point of view, this is a significant feature. The motion of spin-orbit coupled atoms can be manipulated by performing operations on the Zeeman lattice. Moving, accelerating, or shaking a lattice by changing the laser frequency in one of the beams can typically be performed with much higher precision than directly moving the atoms^{1,31}. The restoration of Galilean invariance is, hence, an important aspect. The restoration is specific for the spin-orbit coupled Zeeman lattice. A standard spin-orbit coupled lattice lacks the Galilean invariance. A typical Hamiltonian for a standard spin-orbit coupled optical lattice is^{7,26} $H_{\text{soc}} = p_x^2/2m + \gamma p_x \sigma_z + V_0 \cos^2[x + x_0(t)]$, where γ is the spin-orbit coupling strength, $V_0 \cos^2[x + x_0(t)]$ is the moving optical lattice, and V_0 is the lattice depth. Transforming into the co-moving frame by applying the generalized Galilean transformation results in $G^\dagger H_{\text{soc}} G - i\hbar G^\dagger \partial G/\partial t = p_x^2/2m + \gamma p_x \sigma_z - \gamma m \sigma_z dx_0/dt + V_0 \cos^2(x) + \mathcal{F}x$. The lack of the Galilean invariance is demonstrated by the appearance of the term $\gamma m \sigma_z dx_0/dt$, which depends on the frame velocity dx_0/dt . Physically, the optical lattice generated by optical lattice lasers and the spin-orbit coupling generated by Raman lasers have two independent frames. Working in the co-moving frame with the optical lattice must affect the spin-orbit coupling frame in the way that Raman laser frequencies are Doppler shifted. Therefore it leads to the appearance of an effective detuning $\gamma m \sigma_z dx_0/dt$. The lack of Galilean invariance in this system means that the manipulation of motions of the spin-orbit coupled atoms via the optical lattice is inevitably accompanied by the changing of the spin degree of freedom. For the spin-orbit coupled Zeeman lattice, the frames for the Zeeman lattice and the spin-orbit coupling are not independent. The RF coupling does not produce an additional reference frame for the atoms due to the negligible Doppler shift associated with RF frequencies (see Supplementary Note 1 for details). The Zeeman lattice presented here produces a spin-dependent lattice with a reference frame that only depends on one parameter—the angular frequency difference between Raman lasers $\Delta\omega_R(t)$. Therefore, in our experiments described below we only change $\Delta\omega_R$ and keep ω_{RF} constant.

Bloch oscillation in the Zeeman lattice. To investigate dynamics and exploit the Galilean invariance of the Zeeman lattice, we first consider Bloch oscillations, i.e., the oscillatory motion of particles confined in a periodic potential under the influence of a constant force. Here we explore the band structure shown in Fig. 2(b) where the lowest band is well isolated from the first excited band, suppressing Landau–Zener tunneling³¹.

To experimentally demonstrate Bloch oscillations in the system, we prepare the ground state of the stationary Zeeman lattice (see Materials and methods for details) and then ramp up the frequency difference between the Raman beams in such a way that the relative phase between the two Raman beams evolves as $\varphi(t) = \omega_{\text{RF}}t + \alpha t^2$ with $\alpha = 15\pi \text{ MHz s}^{-1}$, or, in different experimental runs, $\alpha = 15\pi \text{ MHz s}^{-1}$. Therefore the Zeeman lattice is accelerated as $x_0(t) = [\varphi(t) - \omega_{\text{RF}}t]/2k_{\text{R}} = \alpha t^2/2k_{\text{R}}$ with the constant acceleration $\alpha/k_{\text{R}} = 8.24 \text{ m s}^{-2}$, or $\alpha/k_{\text{R}} = -8.24 \text{ m s}^{-2}$, respectively. The velocity of the lattice evolves as $v_{\text{lat}} = \alpha t/k_{\text{R}}$. Equivalently, in the frame of the moving lattice atoms feel a constant force $\mathcal{F} = -m\alpha/k_{\text{R}}$ from the last term in Eq. (5). It linearly changes the quasimomentum of the atoms, $k(t) = -0.97k_{\text{R}} + \mathcal{F}t/\hbar = -0.97k_{\text{R}} - mv_{\text{lat}}/\hbar$. The acceleration is applied for up to 2 ms, which corresponds to moving through more than two Brillouin zones. The ramp can be performed in either direction (i.e., $\pm \alpha$), yielding four Brillouin zones worth of data. At various stages along the ramp, and thus for various lattice velocities, we perform expansion imaging of the BEC and from the observed velocity components determine the average lab-frame velocity v_{lab} of the cloud. The obtained v_{lab} as a function of v_{lat} are presented in Fig. 3a. The staircase structure is the characteristics of Bloch oscillations. In the co-moving frame with the lattice, the lattice is at rest and the BEC has the group velocity, $v_{\text{g}} = v_{\text{lab}} - v_{\text{lat}}$, which forms the sinusoidal pattern as shown in

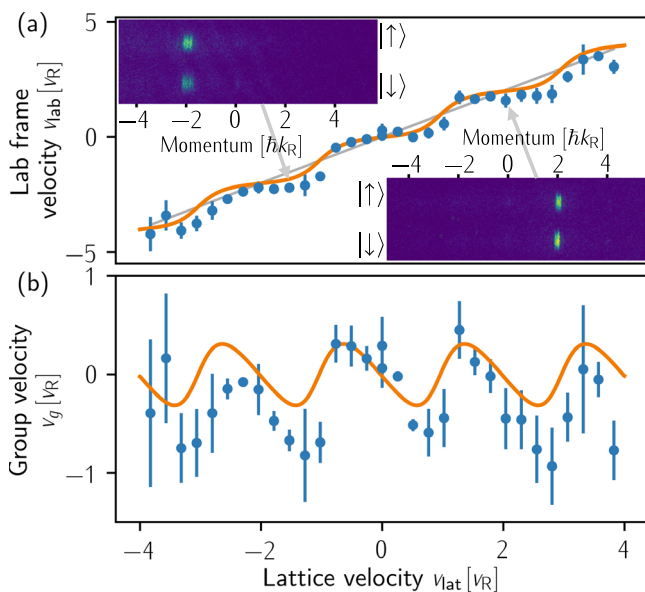


Fig. 3 Bloch oscillations. **a** Velocity in the lab frame versus lattice velocity. The underlying straight line corresponds to $v_{\text{lab}} = v_{\text{lat}}$. The absorption images are taken at two different instances where atoms occupy different spin-momentum states due to Bloch oscillation. **b** Group velocity versus lattice velocity. The blue dots represent the average of three experimental realizations and the orange line represents the theoretical results based on the curvature of the ground state band. The error bars represent the standard deviation of the experimental data. The velocities are reported in units of recoil velocity, $v_{\text{R}} = \hbar k_{\text{R}}/m$, but can equivalently be read as momentum in units of k_{R} . The system was prepared with $\hbar\Omega_{\text{R}} = (2.6 \pm 0.13) E_{\text{R}}$, $\hbar\Omega_{\text{RF}} = (2.3 \pm 0.07) E_{\text{R}}$, $b_z = \hbar \times (500 \pm 100) \text{ Hz}$.

Fig. 3b. In theory, the group velocity can be predicted by calculating the gradient of the lowest band $\epsilon_0(k)$ shown in Fig. 2b, $v_{\text{g}} = \partial\epsilon_0(k)/\hbar\partial k$. The theoretically calculated group velocity is shown by the orange curves in Fig. 3. The good agreement between the observations and theoretical predictions confirms that we can effectively accelerate atoms in the spin-orbit coupled lattice by accelerating the lattice instead.

The condensate atoms experience modulational instability during their Bloch oscillations, resulting in a fringe-like substructure within each momentum class. This instability, influenced by parameters like duration within the unstable region, the system's nonlinearity related to the condensate atom numbers, and external perturbations, leads to random variations in the width of momentum peaks, suggesting no inherent significance to the differences observed in the insets of Fig. 3a.

Band spectroscopy of the Zeeman lattice. Next, we show that a periodic modulation of the frequency difference between the Raman beams leads to a shaken Zeeman lattice, which can induce inter-band transitions. This provides a practical means for performing band spectroscopy in the Zeeman lattice.

We begin with a BEC prepared in the ground state of the stationary Zeeman lattice with $\hbar\Omega_{\text{R}} = (2.6 \pm 0.13) E_{\text{R}}$, $\hbar\Omega_{\text{RF}} = (1.15 \pm 0.03) E_{\text{R}}$, and $b_z = \hbar \times (500 \pm 100) \text{ Hz}$ (see Materials and methods for details and Supplementary Fig 2). To modulate the phase of the lattice¹, we apply a sinusoidal modulation to the Raman frequency difference such that $x_0(t) = [\varphi(t) - \omega_{\text{RF}}t]/2k_{\text{R}} = \phi_0 \sin(2\pi ft)/2k_{\text{R}}$, where $\phi_0/2k_{\text{R}}$ and f are the shaking amplitude and frequency, respectively. In the co-moving frame with the shaken lattice, atoms experience the oscillating force as $\mathcal{F} = 2\pi^2 m \phi_0^2 \sin(2\pi ft)/k_{\text{R}}$. To induce inter-band transition, the amplitude of \mathcal{F} should be a perturbation to the system. We shake the lattice with an amplitude of $\phi_0/2k_{\text{R}} = \pi/20k_{\text{R}}$ for 6 ms using various frequencies f . The measured spin polarization as a function of f is shown in Fig. 4a. The observed response of the spin polarization centered at $f = (2.02 \pm 0.05) \text{ kHz}$ is the signature of an inter-band transition.

Further transitions can be observed by driving the system at higher frequencies. Here, we modulate the phase by $\phi_0/2k_{\text{R}} = \pi/40k_{\text{R}}$ for 2 ms at each frequency. In this case, the clearest signature of the transition is seen in the fractional population of the bare momentum states, which can be understood by inspecting the spin and bare-momentum composition of the underlying bands. The availability of different but correlated observables for the spectroscopy is a particular strength of our Zeeman lattice. Figure 4b shows that the fractional population of the zero-momentum state exhibits a single broad feature, indicating transitions out of the ground band. Plotting the fractional populations in the $\pm 2k_{\text{R}}$ states resolves this broad peak into two peaks centered at $(8.24 \pm 0.04) \text{ kHz}$ and $(8.65 \pm 0.02) \text{ kHz}$, respectively, where the uncertainty in the line center is given by the standard error of the fit to the experimental data.

These observed features are in reasonable agreement with the theory calculations for the excitations to the $n = 1, 2, 3$ states. For a BEC placed at a minimum of the lowest band occurring at the quasimomentum $k = (0.97 \pm 0.02) k_{\text{R}}$, the diagonalization of Eq. (2) for the stationary lattice predicts the $n = 0 \rightarrow 1, 2, 3$ transitions to occur at frequencies 2.05, 8.12, and 8.79 kHz for our experimental parameters, as marked with dashed lines in Fig. 4. These values are calculated based on a two-state model for an infinite, noninteracting, two-state system. We note that the resonance frequencies are quite sensitive to the atomic momentum—displacing the momentum along the noninteracting dispersion by just $0.02 k_{\text{R}}$ produces a near perfect agreement

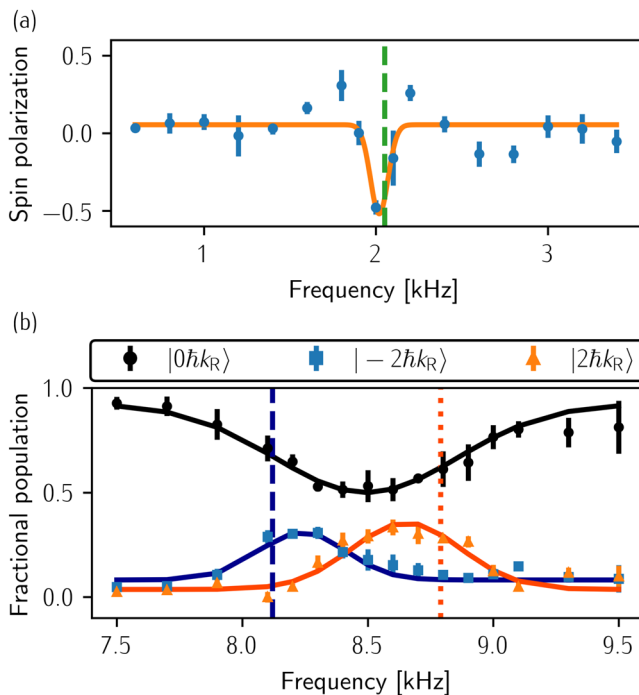


Fig. 4 Lattice band spectroscopy. **a** Spin-polarization as a function of lattice shaking frequency near the $n = 0 \rightarrow 1$ resonance. The blue-filled circles represent the average measured spin polarization, and the solid orange line represents the Gaussian fit to them. The resonance is indicated by a strong spin polarization response. The vertical dashed line corresponds to the predicted resonance frequency calculated for the $n = 0 \rightarrow 1$ transition using an infinite, noninteracting, two-state model. **b** Lattice band spectroscopy measuring the momentum-space response as a function of lattice shaking frequency near the $n = 0 \rightarrow 2, 3$ resonances. The black-filled circles, blue squares, and orange triangles represent the corresponding average measured fractional population, and the solid lines represent the Gaussian fit to them. The vertical dashed and dotted lines correspond to the predicted resonance frequency for the $n = 0 \rightarrow 2$ transitions and $n = 0 \rightarrow 3$ transition, respectively. The error bars represent the standard deviation of the experimental data.

between experiment and theory for all three resonances observed here. The detuning b_z breaks the parity symmetry $\mathcal{P}\sigma_x$ of the stationary spin-orbit coupled Zeeman lattice, where \mathcal{P} is the parity operator with $\mathcal{P}^\dagger x \mathcal{P} = -x$. So the observation of above three band transitions is possible without the constraint of the selection rule due to the parity symmetry (see Supplementary Note 3 for details).

Conclusions

We have studied the rich dynamics of atoms in a spin-orbit coupled Zeeman lattice that emerges from the confluence of spin-orbit coupling and an external radio frequency field. We have discussed the role of Galilean invariance and find that this invariance is restored in the Zeeman lattice, while spin-orbit coupling alone breaks Galilean invariance. This has important consequences for experiments: controlling the motion of the lattice structure is typically much more precise and flexible than controlling the motion of the atoms. We have applied this insight to characterize the Zeeman lattice using Bloch oscillations and resonant band spectroscopy. In our band spectroscopy, we have shown that both spin and momentum composition are useful observables, demonstrating the multifaceted nature of the Zeeman lattice. The availability of a variety of correlated observables, such as spin and momentum populations, affords powerful

experimental tools for performing detailed studies. This work shows that the spin-orbit coupled Zeeman lattice introduced in^{23,24} provides powerful methods for further investigations of spin-orbit coupling including spin-dependent lattices, the characterization of a semimetal-like band structure (Fig. 2c), dynamics of a BEC in a tunable flat ground band (Fig. 2d), the realization of Wannier-Stark ladders³⁴, and exploration of the spin Hall effect³⁵, to name a few.

Methods

Experimental setup. In our experiment, we prepare a BEC of approximately 2.5×10^{587} Rb atoms in the $|F, m_F\rangle = |1, -1\rangle$ Zeeman state. The BEC is confined in a crossed optical dipole trap characterized by the harmonic trap frequencies $\omega = (\omega_x, \omega_y, \omega_z) = 2\pi(20 \pm 2, 160 \pm 10, 190 \pm 10)$ Hz. A $10 \text{ G} \pm 0.1 \text{ mG}$ bias field applied along the x -axis lifts the degeneracy among the three states in the $F = 1$ hyperfine manifold. We generate spin-orbit coupling in the x -direction using two Raman beams with a wavelength of 789 nm intersecting at approximately 45° angles with the x -axis, as shown in Fig. 1b. This leads to an effective recoil energy of $E_R = h \times 1.9$ kHz. The frequencies of the Raman beams are tuned such that the $|1, -1\rangle$ and $|1, 0\rangle$ states are nearly resonantly coupled via the two-photon Raman transition. These two states are additionally coupled by an RF drive (Fig. 1a). The quadratic Zeeman shift places the $|1, +1\rangle$ state far out of resonance so that effectively a spin-1/2 system composed of $|\uparrow\rangle \equiv |1, -1\rangle$ and $|\downarrow\rangle \equiv |1, 0\rangle$ as the two pseudo-spin states is realized. After performing the experiments described in the previous sections, imaging is performed by suddenly turning off the trap and all driving fields, and allowing time of flight in the presence of a Stern-Gerlach field. An absorption image is then taken which resolves the BEC into the bare-state spin and momentum components. The existence of lattice structure has been experimentally detected by Kapitza-Dirac scattering²³ (see Supplementary Note 2 for details and Supplementary Fig. 1).

Zeeman lattice ground state preparation. We begin an experiment by preparing the BEC in a minimum of the lowest band of the stationary Zeeman lattice: we adiabatically dress the condensate with a Raman coupling field of strength $\hbar\Omega_R = (2.6 \pm 0.13) E_R$ and a detuning $b_z = h \times (500 \pm 100)$ Hz, and then adiabatically ramp on the strength of the radio frequency drive to a coupling strength of $\hbar\Omega_{\text{RF}} = (2.3 \pm 0.07) E_R$ over 100 ms while satisfying the stationary lattice condition $\varphi - \omega_{\text{RF}}t = 0$.

Data availability

All data in the main text or the supplementary materials are available upon reasonable request.

Received: 5 March 2023; Accepted: 15 December 2023;

Published online: 05 January 2024

References

- Denschlag, J. H. et al. A Bose-Einstein condensate in an optical lattice. *J. Phys. B* **35**, 3095–3110 (2002).
- Morsch, O. & Oberthaler, M. Dynamics of Bose-Einstein condensates in optical lattices. *Rev. Mod. Phys.* **78**, 179–215 (2006).
- Bloch, I., Dalibard, J. & Zwirger, W. Many-body physics with ultracold gases. *Rev. Mod. Phys.* **80**, 885–964 (2008).
- Jo, G.-B. et al. Ultracold atoms in a tunable optical Kagome lattice. *Phys. Rev. Lett.* **108**, 045305 (2012).
- Lin, Y.-J., Jiménez-García, K. & Spielman, I. B. Spin-orbit-coupled Bose-Einstein condensates. *Nature* **471**, 83–86 (2011).

6. Higbie, J. & Stamper-Kurn, D. M. Generating macroscopic-quantum-superposition states in momentum and internal-state space from Bose-Einstein condensates with repulsive interactions. *Phys. Rev. A* **69**, 053605 (2004).
7. Hamner, C., Zhang, Y., Khamehchi, M. A., Davis, M. J. & Engels, P. Spin-orbit-coupled Bose-Einstein condensates in a one-dimensional optical lattice. *Phys. Rev. Lett.* **114**, 070401 (2015).
8. An, F. A., Meier, E. J., Ang'ong'a, J. & Gadway, B. Correlated dynamics in a synthetic lattice of momentum states. *Phys. Rev. Lett.* **120**, 040407 (2018).
9. Huang, L. et al. Experimental realization of two-dimensional synthetic spin-orbit coupling in ultracold Fermi gases. *Nat. Phys.* **12**, 540–544 (2016).
10. Cooper, N. R. Optical flux lattices for ultracold atomic gases. *Phys. Rev. Lett.* **106**, 175301 (2011).
11. Li, C. et al. Topological edge states in Rashba-Dresselhaus spin-orbit-coupled atoms in a Zeeman lattice. *Phys. Rev. A* **98**, 061601 (2018).
12. Zhang, W., Chen, X., Kartashov, Y. V., Konotop, V. V. & Ye, F. Coupling of edge states and topological bragg solitons. *Phys. Rev. Lett.* **123**, 254103 (2019).
13. Bersano, T. M. et al. Experimental realization of a long-lived striped Bose-Einstein condensate induced by momentum-space hopping. *Phys. Rev. A* **99**, 051602 (2019).
14. Li, J.-R. et al. A stripe phase with supersolid properties in spin-orbit-coupled Bose-Einstein condensates. *Nature* **543**, 91–94 (2017).
15. Han, W. et al. Chiral supersolid in spin-orbit-coupled Bose gases with soft-core long-range interactions. *Phys. Rev. Lett.* **121**, 030404 (2018).
16. Zhu, Q., Zhang, C. & Wu, B. Exotic superfluidity in spin-orbit coupled Bose-Einstein condensates. *Eur. Phys. Lett.* **100**, 50003 (2012).
17. Huang, L. et al. Observation of Floquet bands in driven spin-orbit-coupled Fermi gases. *Phys. Rev. A* **98**, 013615 (2018).
18. Nadj-Perge, S., Frolow, S. M., Bakkers, E. P. A. M. & Kouwenhoven, L. P. Spin-orbit qubit in a semiconductor nanowire. *Nature* **468**, 1084–1087 (2010).
19. Huang, Y.-X. et al. Bose-Einstein condensate in Bloch bands with an off-diagonal periodic potential. *Phys. Rev. A* **100**, 053606 (2019).
20. Xu, Y., Zhang, Y. & Zhang, C. Bright solitons in a two-dimensional spin-orbit-coupled dipolar Bose-Einstein condensate. *Phys. Rev. A* **92**, 013633 (2015).
21. Zhang, Y.-C. et al. Superfluid density of a spin-orbit-coupled Bose gas. *Phys. Rev. A* **94**, 033635 (2016).
22. Kartashov, Y. V., Konotop, V. V., Zezyulin, D. A. & Torner, L. Bloch oscillations in optical and Zeeman lattices in the presence of spin-orbit coupling. *Phys. Rev. Lett.* **117**, 215301 (2016).
23. Jiménez-García, K. et al. Peierls substitution in an engineered lattice potential. *Phys. Rev. Lett.* **108**, 225303 (2012).
24. Cheuk, L. W. et al. Spin-injection spectroscopy of a spin-orbit coupled Fermi gas. *Phys. Rev. Lett.* **109**, 095302 (2012).
25. Lu, H.-I. et al. Geometrical pumping with a Bose-Einstein condensate. *Phys. Rev. Lett.* **116**, 200402 (2016).
26. Zhang, S., Cole, W. S., Paramekanti, A. & Trivedi, N. Spin-orbit coupling in optical lattices. *Annu. Rev. Cold At. Mol.* **3**, 135 (2015).
27. Zhang, Y. & Zhang, C. Bose-Einstein condensates in spin-orbit-coupled optical lattices: flat bands and superfluidity. *Phys. Rev. A* **87**, 023611 (2013).
28. Zhang, J.-Y. et al. Collective dipole oscillations of a spin-orbit coupled Bose-Einstein condensate. *Phys. Rev. Lett.* **109**, 115301 (2012).
29. Geissler, F., Crépin, F. & Trauzettel, B. Evidence for broken Galilean invariance at the quantum spin Hall edge. *Phys. Rev. B* **92**, 235108 (2015).
30. Zhu, Q.-Z. & Wu, B. Superfluidity of Bose-Einstein condensates in ultracold atomic gases. *Chin. Phys. B* **24**, 050507 (2015).
31. Peik, E., Ben Dahan, M., Bouchoule, I., Castin, Y. & Salomon, C. Bloch oscillations of atoms, adiabatic rapid passage, and monokinetic atomic beams. *Phys. Rev. A* **55**, 2989–3001 (1997).
32. Kovachy, T., Hogan, J. M., Johnson, D. M. S. & Kasevich, M. A. Optical lattices as waveguides and beam splitters for atom interferometry: an analytical treatment and proposal of applications. *Phys. Rev. A* **82**, 013638 (2010).
33. Messiah, A. *Quantum Mechanics*. (Dover Publications, Newburyport, 2014).
34. Wilkinson, S. R., Bharucha, C. F., Madison, K. W., Niu, Q. & Raizen, M. G. Observation of atomic Wannier-Stark ladders in an accelerating optical potential. *Phys. Rev. Lett.* **76**, 4512–4515 (1996).
35. Li, C.-H. et al. Bose-Einstein condensate on a synthetic topological hall cylinder. *PRX Quantum* **3**, 010316 (2022).

Acknowledgements

M.K.H.O., A.M., E.C., S.M., T.B., and P.E. acknowledge funding from NSF through Grant No. PHY-1912540. P. E. acknowledges support through the Ralph G. Yount Distinguished Professorship at WSU. H.H. and Y.Z. are supported by National Natural Science Foundation of China with Grants Nos. 12374247 and 11974235.

Author contributions

P.E. and Y.Z. conceived and supervised the research project. Y.Z., H.H., S.M., E.C., and M.K.H.O. performed the theoretical analysis and numerics. P.E., S.M., T.B., E.C., M.K.H.O., and A.M. did the experiment, data analysis, and interpretation. All authors discussed the results and contributed to the paper preparation, review, and editing.

Competing interests

The authors declare no competing interests.

Additional information

Supplementary information The online version contains supplementary material available at <https://doi.org/10.1038/s42005-023-01506-4>.

Correspondence and requests for materials should be addressed to Yongping Zhang or P. Engels.

Peer review information *Communications Physics* thanks Erich Mueller and the other anonymous reviewer(s) for their contribution to the peer review of this work.

Reprints and permission information is available at <http://www.nature.com/reprints>

Publisher's note Springer Nature remains neutral with regard to jurisdictional claims in published maps and institutional affiliations.



Open Access This article is licensed under a Creative Commons Attribution 4.0 International License, which permits use, sharing, adaptation, distribution and reproduction in any medium or format, as long as you give appropriate credit to the original author(s) and the source, provide a link to the Creative Commons licence, and indicate if changes were made. The images or other third party material in this article are included in the article's Creative Commons licence, unless indicated otherwise in a credit line to the material. If material is not included in the article's Creative Commons licence and your intended use is not permitted by statutory regulation or exceeds the permitted use, you will need to obtain permission directly from the copyright holder. To view a copy of this licence, visit <http://creativecommons.org/licenses/by/4.0/>.

© The Author(s) 2024